Supporting Information

Bimetallic ZnCo-MOF derived porous Ir-doped cobalt oxides for water oxidation with improved activity and stability

Junliang Chen, Jie Liu, Shaojie Xu, Yi Wu, Yunan Ye and Jinjie Qian*****

Key Laboratory of Carbon Materials of Zhejiang Province, College of Chemistry and Materials Engineering, Wenzhou University, Wenzhou 325035, Zhejiang, P. R. China

*Corresponding author

E-mail: jinjieqian@wzu.edu.cn (J. Qian)

Experimental Section

Chemicals and Reagents

All chemicals are purchased and used without further purification. Cobalt(II) acetate tetrahydrate ($Co(CH_3COO)_2 \cdot 4H_2O$, AR), zinc acetate dihydrate ($Zn(CH_3COO)_2 \cdot 2H_2O$, AR), 2-methylimidazole (2-HMeIm, AR, 99%), sodium hydroxide (NaOH, 95%), iridium trichloride hydrate ($IrCl_3 \cdot xH_2O$, AR), and ethanol (EtOH, moisture content ≤0.3% and ≤0.1%) are purchased from Shanghai Aladdin Corporation. 5 wt% Nafion ionomers are purchased from Aldrich. All the salts, solvents and other reagents are of analytical grade. High-purity N_2, Ar gases, and deionized water (18.2 MΩ) are used in all experiments.

Synthesis of ZIF-ZnCo-n (n = 1-4) series, ZIF-Zn and ZIF-Co

7.5 g 2-methylimidazole (2-MI) was first dissolved into 50 mL deionized water with stirring in 400 rpm. Then 12 mmol mixture of $Co(CH_3COO)_2 \cdot 4H_2O$ and $Zn(CH_3COO)_2 \cdot 2H_2O$ (mol% of Zn was in 10, 30, 50, 70, respectively) was added into the above solution and keep agitating for 30 min. After that, the obtained solution was kept in room temperature without stirring for 12 h. Finally, the powder was collected by centrifugation and washed with water and ethanol to remove residual 2-IM and unreacted metal cations. (The obtained samples are denoted as ZIF-ZnCo-1, ZIF-ZnCo-2, ZIF-ZnCo-3, ZIF-ZnCo-4, respectively). The ZIF-Zn and ZIF-Co were synthesized with the same method except for adding Co/Zn salt, respectively.

Synthesis of ZCO-n (n = 1-4) series, CO and ZO

The as-prepared ZIF-ZnCo-n series, ZIF-Co and ZIF-Zn were weighted and placed in the muffle furnace. Then the temperature was set to 300 °C at a heating rate of 5 °C min^{-1} in air atmosphere and maintained for 6 h. The black powder was obtained after cooling to room temperature, denoted as ZCO-1, ZCO-2, ZCO-3, ZCO-4 and CO. Additionally, the obtained white powder derived from ZIF-Zn was denoted as ZO.

Synthesis of pZCO-n (n = 1-4) series

The ZCO-n series and CO (50 mg) were soaked in the NaOH solution (2 M, 20 mL) and stirring for 30 min. After that, the powder was collected by centrifugation and washed with water to remove residual NaOH. The obtained samples were named as pZCO-1, pZCO-2, pZCO-3, pZCO-4 and pCO respectively.

Synthesis of Ir-pZCO

The pZCO-3 (10 mg) was first dispersed homogeneously in 10 mL deionized water. Then 1 mg IrCl$_3$·xH$_2$O was added into the above solution, which was subsequently kept at 60 °C for 9 h under stirring in 600 rpm. After that, the powder was collected by centrifugation and washed with water to remove unreacted metal cations. Moreover, the obtained sample was annealed in the muffle furnace at 250 °C with a heating rate of 5 °C min^{-1} in air atmosphere and maintained for 1 h. The final material was named as Ir-pZCO.

Etching condition exploration

A series of NaOH solutions with different concentrations (0.1 M, 0.2 M, 0.5 M, 1.0 M, 2.0 M) were first prepared and transferred 5 mL into 20 mL glass bottle. Then, the as-prepared ZO (20 mg) was added into the above solutions with stirring at different temperatures and reacted for certain time. The relative photographs were shown below in **Figure S1**.

Material Characterization

The morphology of the samples is analyzed using a Nova NanoSEM 200 scanning electron microscope (FE-SEM, FEI Inc.). N_2 adsorption study is measured in the Specific Surface Area & Pore Size Analyzer (BSD-PS1, Beishide Instrument Technology (Beijing) Co., Ltd.)), where the samples after the activation of the high temperatures are placed in a clean ultra-high vacuum system and the cryogenic temperature of 77 K. The structure and properties are characterized using transmission electron microscopy (TEM, JEOL JEM-2100F microscope), as well as the high-resolution transmission electron microscope (HR-TEM) image and energy Dispersive X-ray spectroscopy (EDS) pattern. Powder X-ray diffraction (PXRD) maps of the products were acquired on a Bruker (Karlsruhe, Germany) D8 Advance powder diffractometer at room temperature, operating at 40 kV, 40 mA, graphite monochromated Cu Kα radiation ($\lambda = 1.54$ Å). X-ray photoelectron spectroscopy (XPS) is conducted on PHI 5000 VersaProbe III. The loading Ir content was detected by inductively coupled plasma optical emission spectroscopy (ICP-OES; NeexlON 2000)

Electrochemical measurements

The electrochemical experiments are carried out at room temperature using a CHI 760E electrochemical station for OER. The experiment used the electrodes of Hg/HgO and platinum net are sequentially behaved as the reference (RE) and counter electrodes (CE), which are used in 1.0 M KOH electrolyte solution. According to a formula $E_{RHE} = E_{SCE} + 0.098\ V + 0.059\ V \times pH = E_{SCE} + 0.912$, all of its potentials can be corrected to reversible hydrogen electrode (RHE) potentials. The catalyst powder (5 mg) is dispersed in a mixture solution of 500 μL (300 μL EtOH, 150 μL deionized water, and 50 μL 5 wt % Nafion solution) and ultrasonicated for 2 h to form a homogeneous catalyst ink. Thereafter, the surface of glassy carbon (diameter: 3 mm) is loaded with 5 μL of a catalyst ink, wherein 0.7 mg cm^{-2} is calculated the loading amount. Linear sweep voltammetry (LSV) is conducted in electrolyte solution without correction (a scan rate: 5 mV s^{-1}). The Tafel slope is transferred according to Tafel equation as follows: $\eta = b \times \log(j\ /\ j_0)$. Regarding the evaluation of the electrochemical active surface areas (ECSA) of the samples, CV has also been performed by measuring the double-layer capacitances (C_{dl}) with various scan rates (20, 40, 60, 80, 100 and 120 mV s^{-1}) under the potential window of 1.05 - 1.15 V *vs.* RHE. The Nyquist plots of EIS are collected from 10^6 Hz to 0.01 Hz with an amplitude of 5 mV at 1.6 V vs. RHE in 1.0 M KOH. For evaluating the long-term performance, the electrochemical stability of the Ir-pZCO is conducted at a constant overpotential of 1.53 V for achieving a high initial current density. In order to calculate the electron transfer number (N), rotating ring-disk electrode (RRDE) voltammogram of as-prepared samples are conducted to collect disk current (I_{disk}) and ring current (I_{ring}) at the same time, equation as follows: $N = 4 \times I_d\ /\ (I_d$

+ I_r / N_c), where I_r is the ring current, I_d is the disk current, and N_c is the current collection efficiency. The Faradaic efficiency (ε) is calculated by the equation as follows: $\varepsilon = I_r /(I_d \cdot N_c)$.

Density functional theory

The density functional theory was used to carry out all the calculations with the Perdew-Burke-Ernzerh exchange-correlation functional of generalized gradient approximation and the projector-augmented wave method, which was implemented through Vienna Ab-initio Simulation Package (VASP).The input model structure file was created by VESTA.[1] The plane wave-basis expansion cutoff energy was fixed at 500 eV, and atomic relaxation was conducted until the force exerted on atoms was less than 0.02 eV Å^{-1} and energy was concurrently converged to 1×10^{-5} eV. The k-point was a Monkhorst-Pack of $3\times3\times1$.
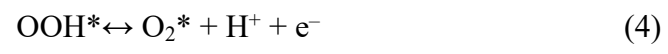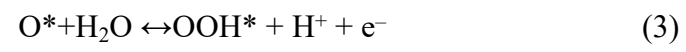
The Gibbs free energy change (ΔG) of each lithiation step was defined as:

$$\Delta G = \Delta E + \Delta ZPE - T\Delta S,$$

where ΔE is the electronic energy difference directly obtained from DFT calculations, ΔZPE is the change in zero-point energy, T is the temperature (T= 298.15 K) and ΔS is the change in the entropy, respectively.[2] The zero-point energy and entropy were obtained through vibrational frequencies.

Conventionally, in an alkaline electrolyte, the anode reactions after oxygen adsorption can be written as:
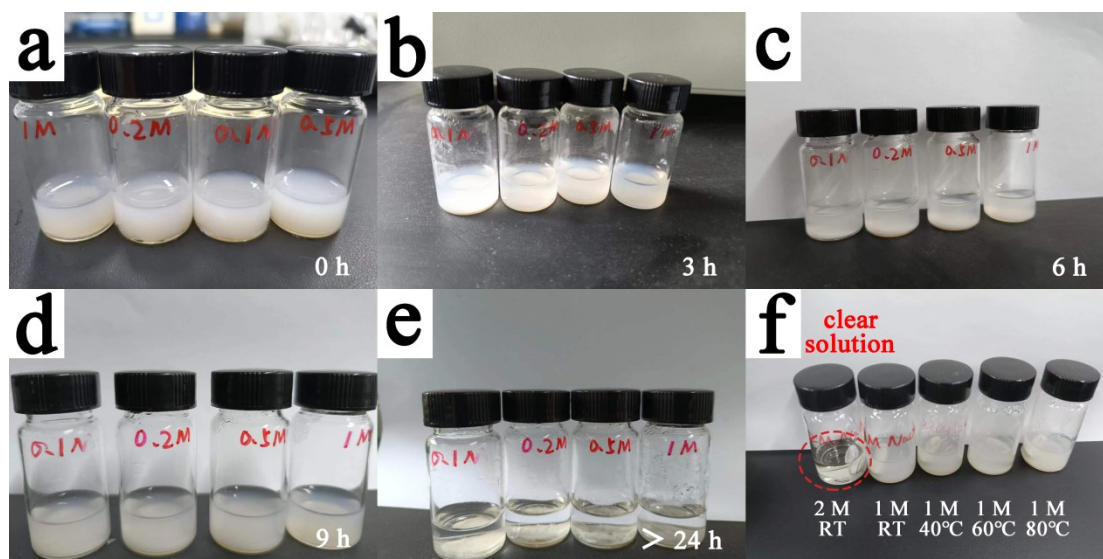
$$H_2O \leftrightarrow OH^* + H^+ + e^- \qquad\qquad (1)$$

$$OH* \leftrightarrow O* + H^+ + e^- \qquad (2)$$

$$O* + H_2O \leftrightarrow OOH* + H^+ + e^- \qquad (3)$$

$$OOH* \leftrightarrow O_2* + H^+ + e^- \qquad (4)$$

Figure S1. The photographs of pure ZnO with base-etching process. (a-e) The ZnO immersed in NaOH solutions with various concentrations (marked on bottle) and reacted at room temperature (RT) for 0 h, 3 h, 6 h, 9 h and > 24 h, respectively. (f) The ZnO immersed in NaOH solutions with various concentrations and reacted at different temperatures (marked in photo) for 0.5 h.

It could be obviously observed that when the concentration was lower than 2.0 M (0.1 M, 0.2 M, 0.5 M, 1.0 M), the ZnO particles were not able to fully dissolve, no matter at what temperature. However, when applied with 2.0 M NaOH, the ZnO rapidly dissolved and formed a clear solution. Therefore, the optimized concentration of 2.0 M NaOH solution was selected for subsequent etching process.
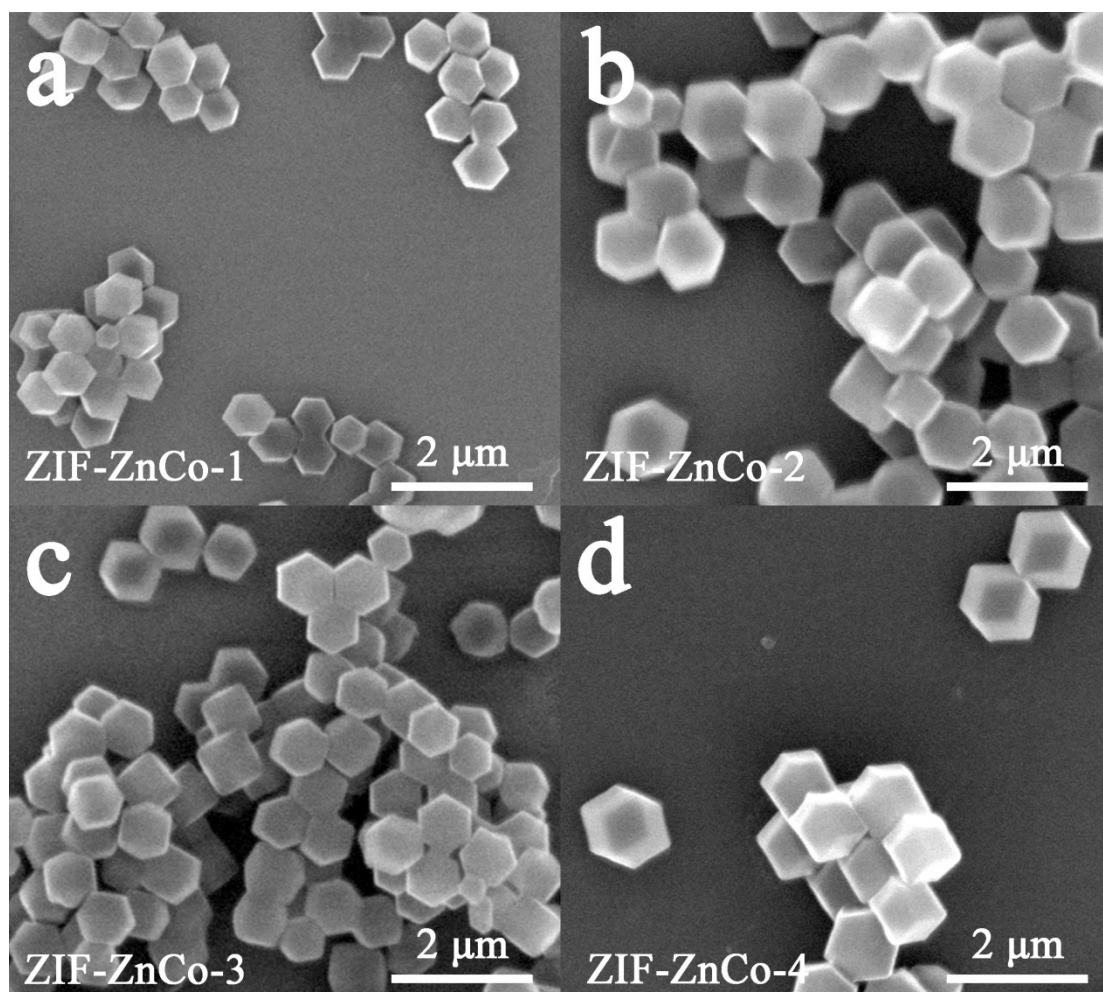
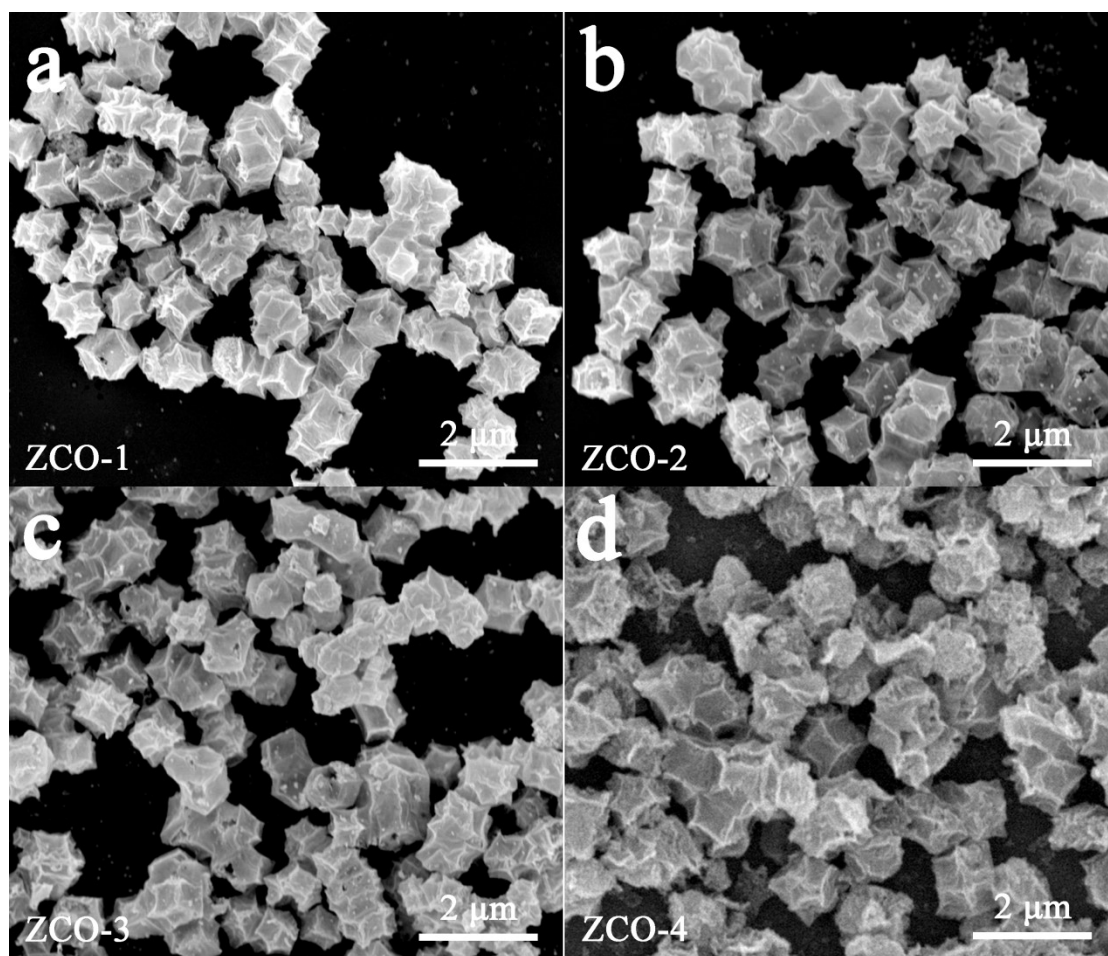**Figure S2**. The SEM images of (a-d) ZIF-ZnCo-1/2/3/4 with various Zn concentrations.

Figure S3. The SEM images of (a-d) ZCO-1/2/3/4 calcined from ZIF-ZnCo-1/2/3/4
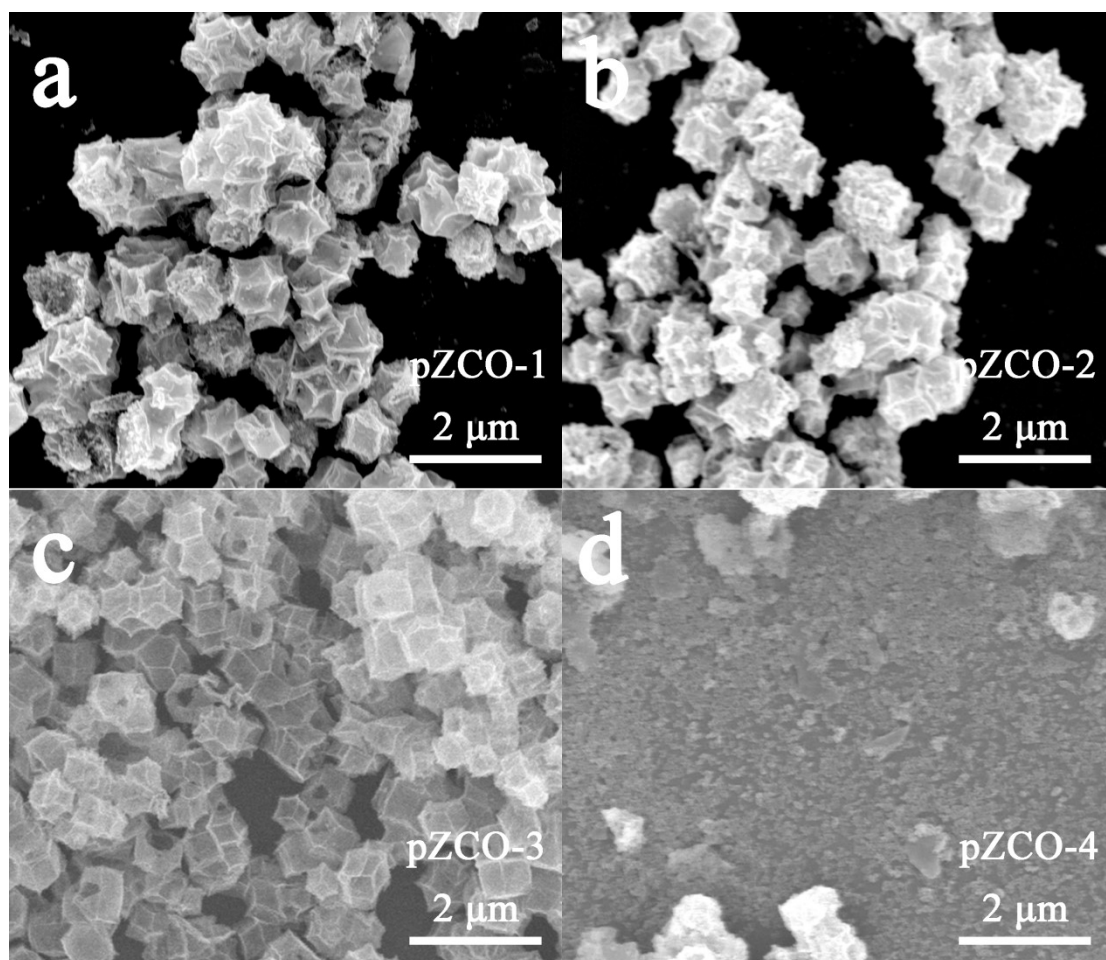
precursors.

Figure S4. The SEM images of (a-d) pZCO-1/2/3/4 base-etched from ZCO-1/2/3/4 precursors.
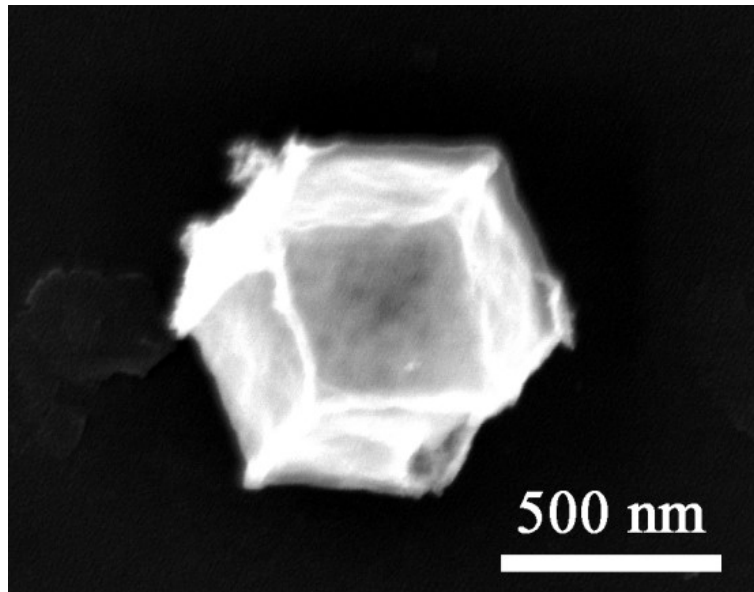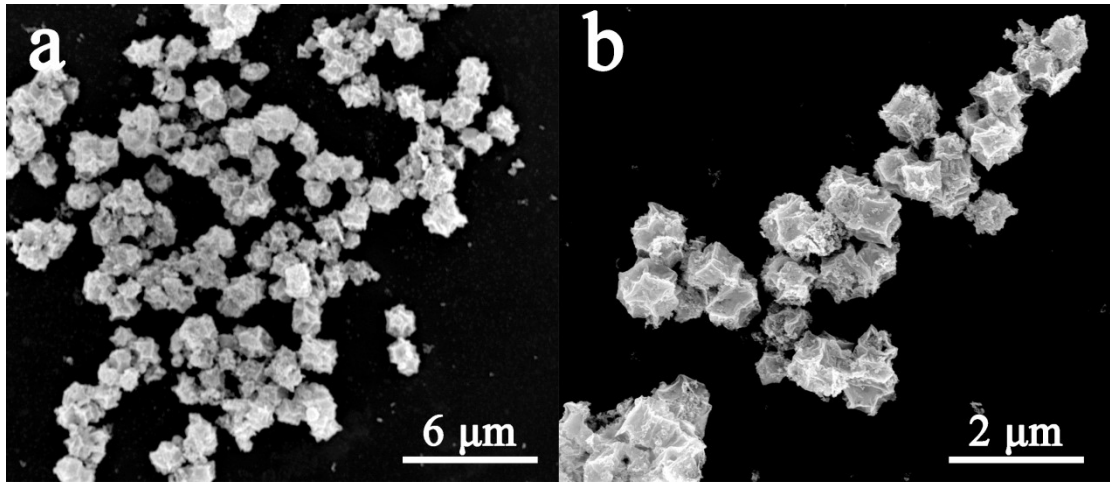
Figure S5. The SEM images of pCO.

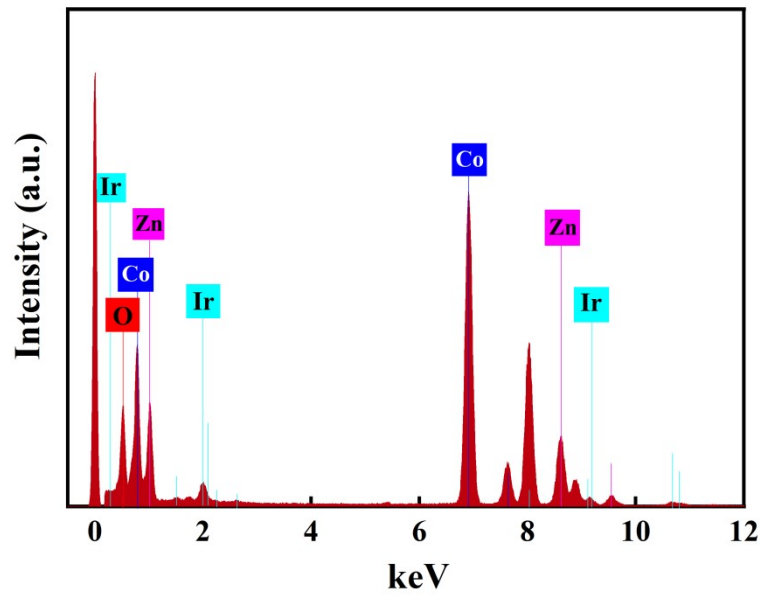**Figure S6**. The SEM images of Ir-pZCO.

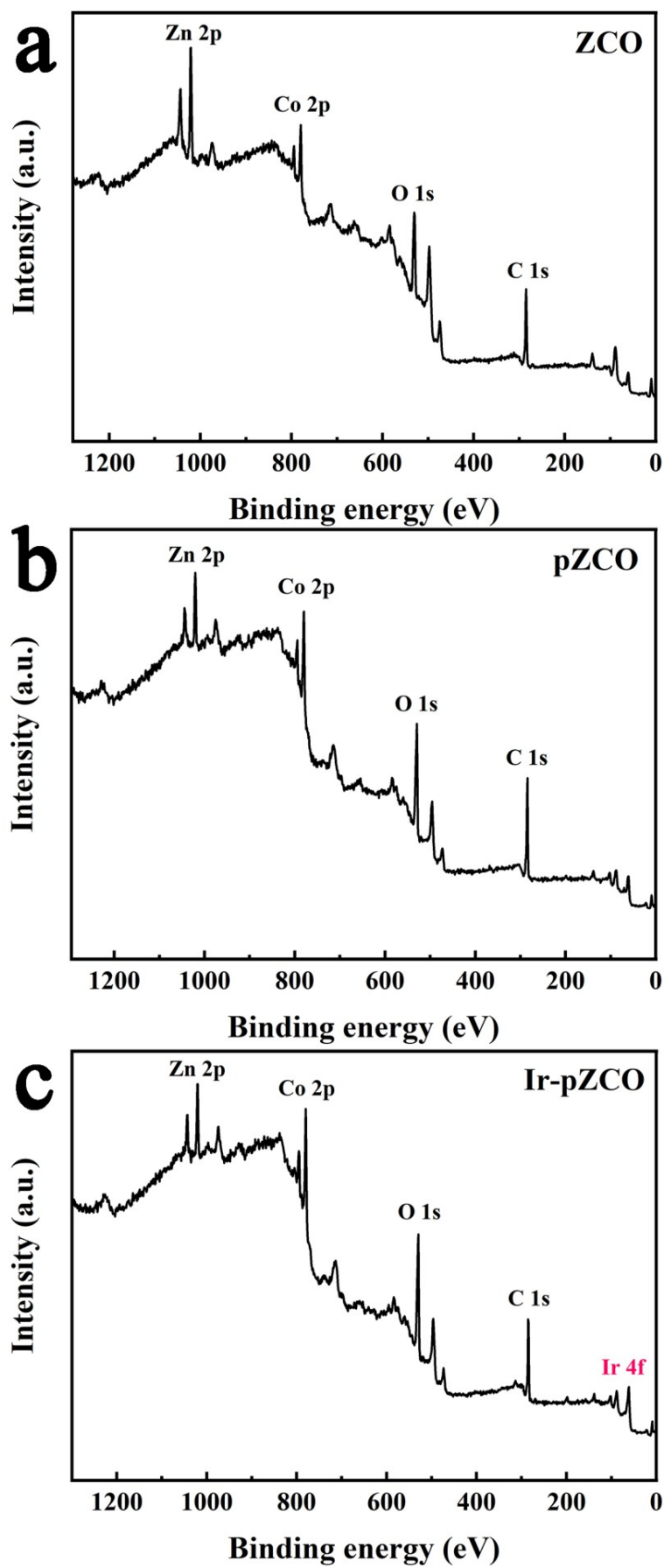**Figure S7**. The EDS pattern of Ir-pZCO.

Figure S8. The full survey XPS spectra of (a) ZCO, (b) pZCO and (c) Ir-pZCO.
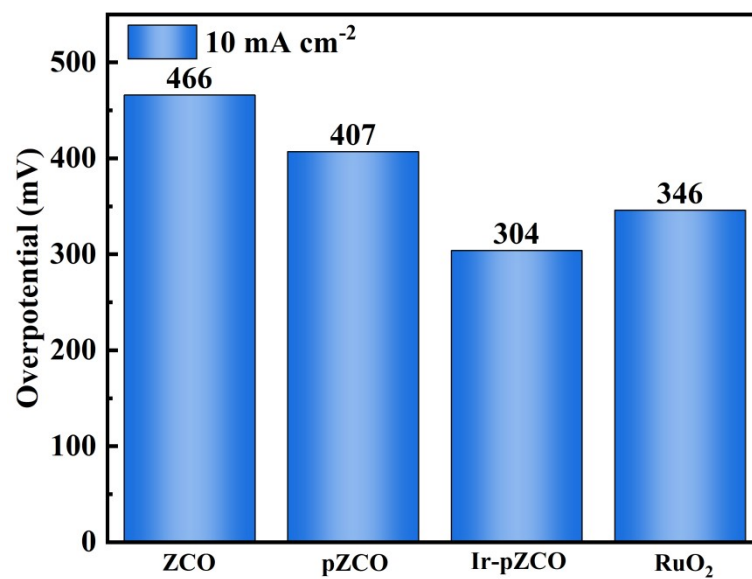
Figure S9. A summary of overpotentials of ZCO, pZCO, Ir-pZCO and RuO_2 at 10 mA

cm^{-2}
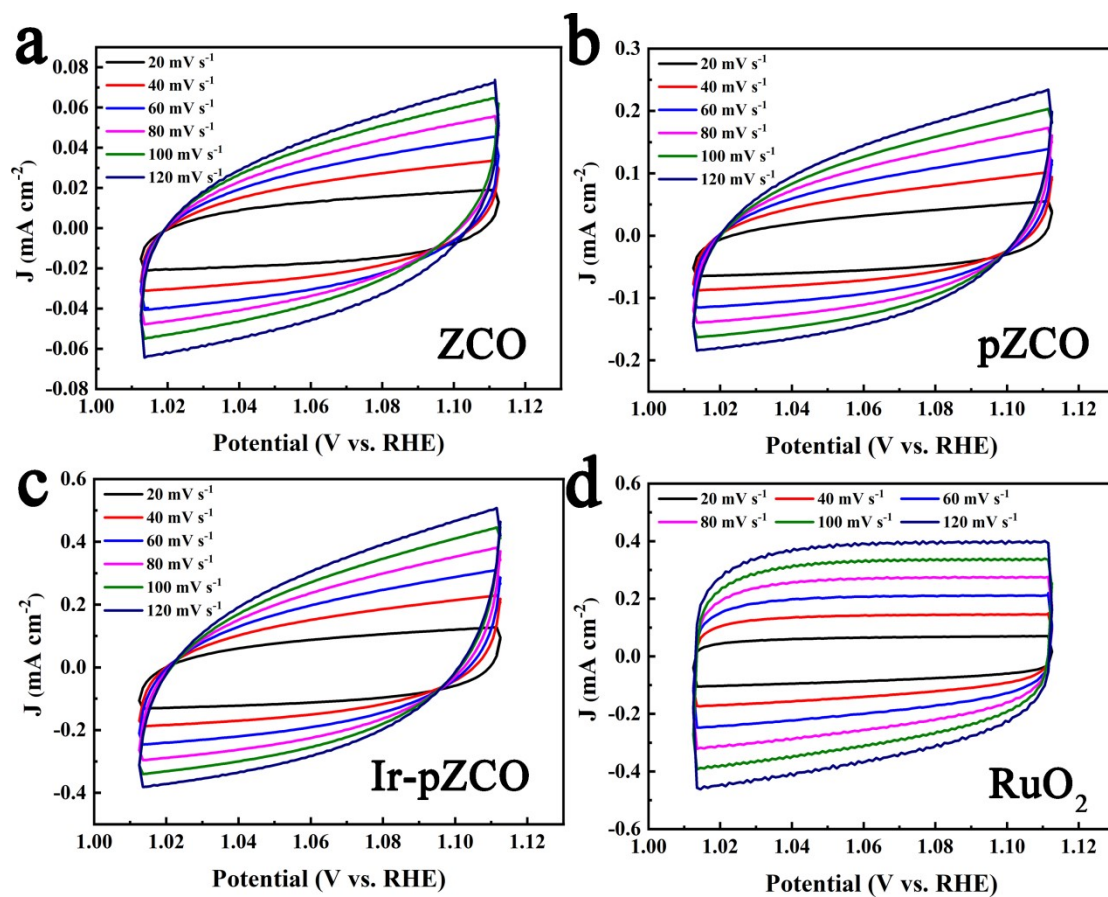
Figure S10. CV curves from 20 to 120 mV s^{-1} for (a) ZCO, (b) pZCO, (c) Ir-pZCO, and (d) RuO$_2$ in 1.0 M KOH.
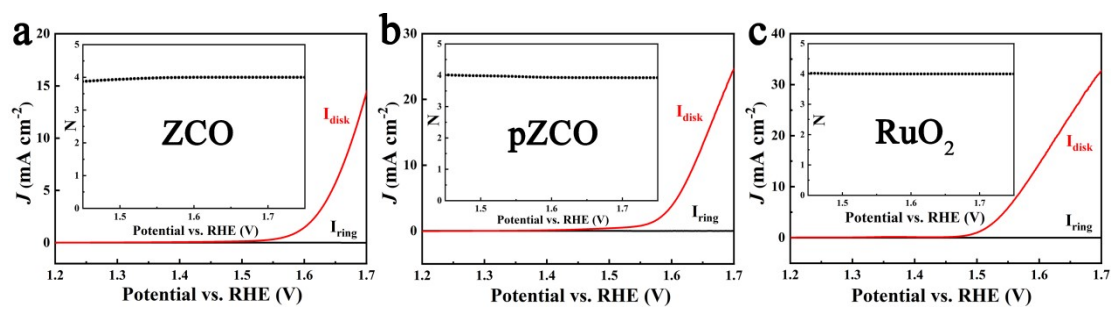
Figure S11. RRDE LSV curves of (a) ZCO, (b) pZCO and (c) RuO$_2$.
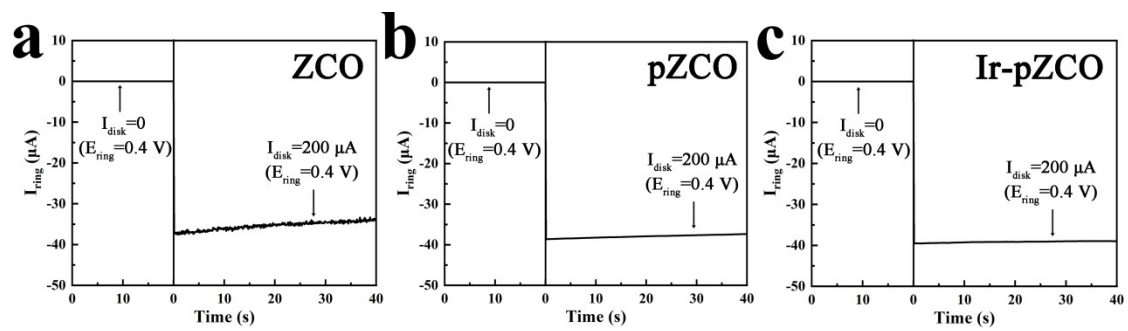
Figure S12. (a-c) the time-dependent ring current of ZCO, pZCO and Ir-pZCO via

RRDE technique.
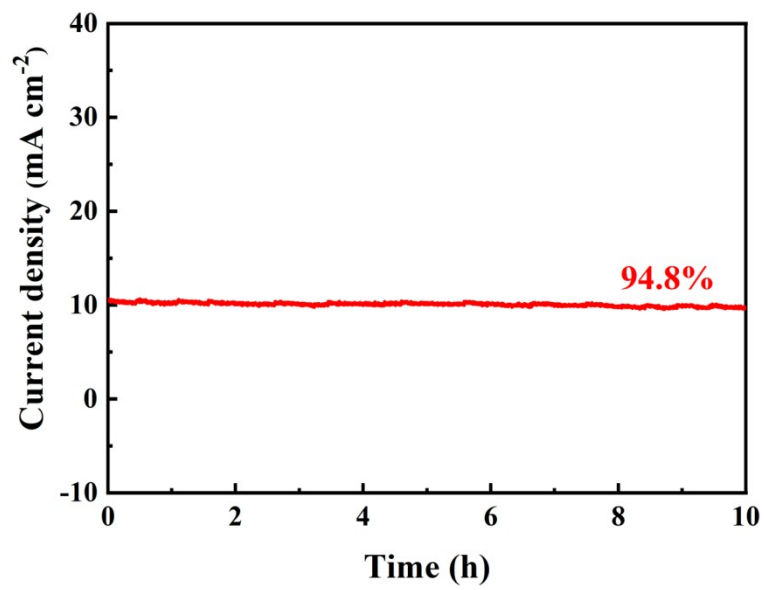
Figure S13. The stability evaluation of Ir-pZCO after 10 hours.
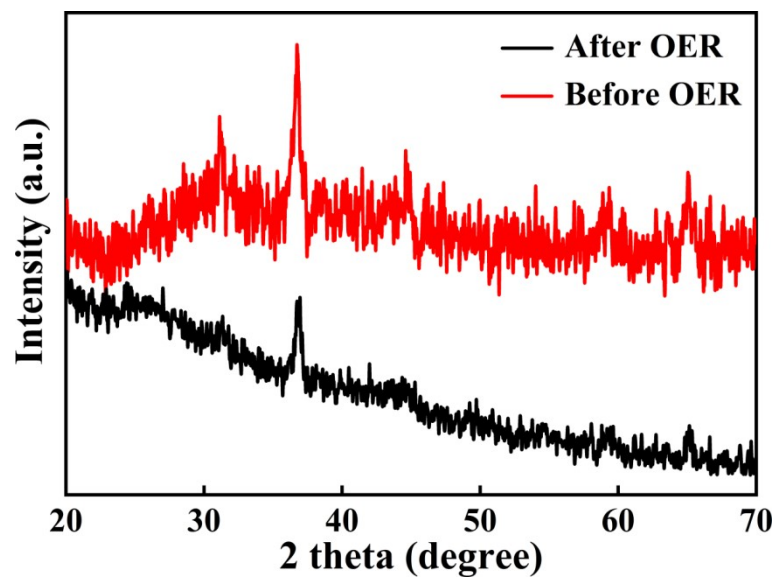
Figure S14. The PXRD patterns of Ir-pZCO before/after the 10-hour OER test.
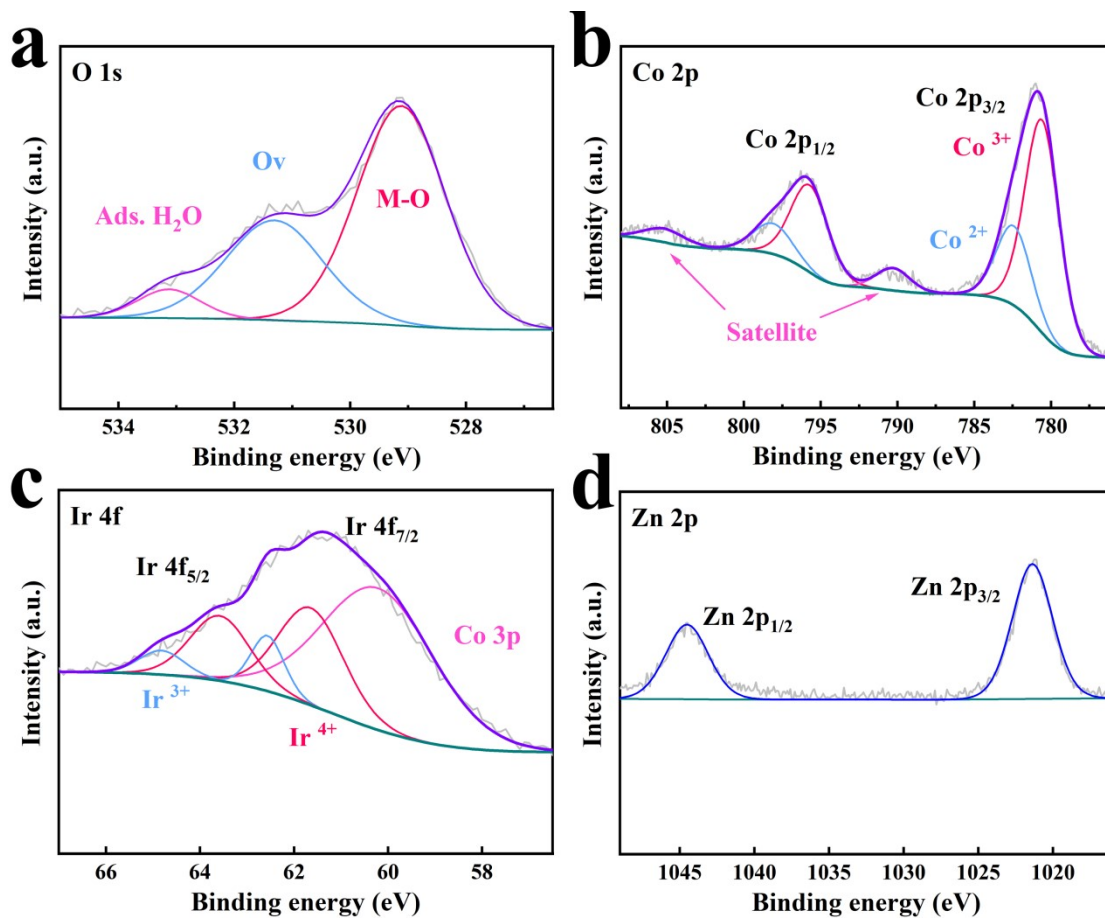
Figure S15. The deconvoluted XPS spectra of Ir-pZCO after OER test.
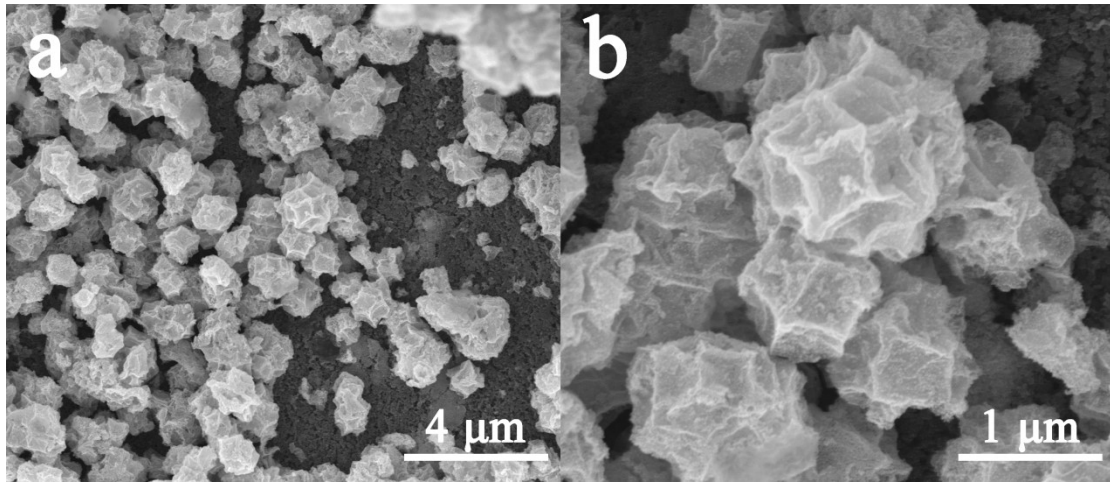
Figure S16. The SEM images of Ir-pZCO after OER.
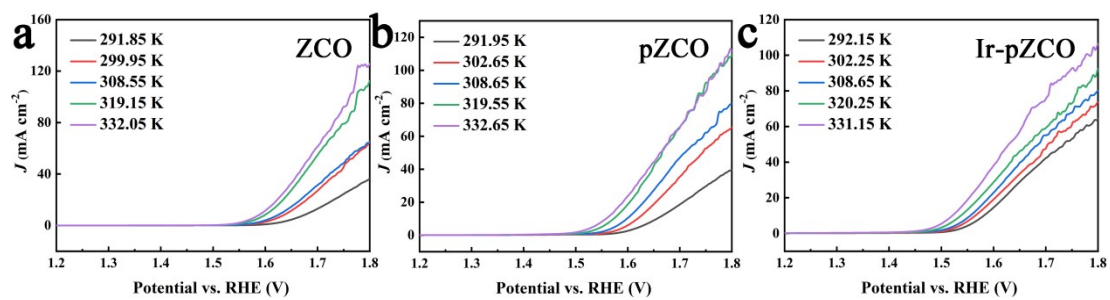
Figure S17. Temperature-dependent LSV curves of (a) ZCO, (b) pZCO, and (c) Ir-pZCO measured in 1.0 M KOH with a sweep rate of 5 mV s^{-1}.

Table S1. Summary of Crystal Data and Refinement Results for ZIF-8.

Compound	ZIF-8[Ref. 3]
Chemical formula	$C_{18}H_8Co_2O_{12}$
Formula mass	746.7
Crystal system	Cubic
Space group	*I*-43m
a (Å)	16.993(2)
b (Å)	16.993(2)
c (Å)	16.993(2)
α (°)	90
β (°)	90
γ (°)	90
Unit cell volume (Å³)	4906.8(10)
Temperature (K)	240(2)
Z	4
R_1 (I>2σ(I))	0.0510
wR (all reflections)	0.1424

Ref. 3.[3] W. Morris, C. J. Stevens, R. E. Taylor, C. Dybowski, O. M. Yaghi, M. A. Garcia-Garibay. NMR and X-ray Study Revealing the Rigidity of Zeolitic Imidazolate Frameworks. *J. Phys. Chem. C.*, **2012**, 116, 13307-13312.

Table S2. Summary of Crystal Data and Refinement Results for ZIF-67.

Compound	ZIF-67[Ref. 4]
Chemical formula	$C_{24}H_{30}N_{12}O_2Co_3$
Crystal system	Cubic
Space group	I-43m
a (Å)	16.959(3)
b (Å)	16.959(3)
c (Å)	16.959(3)
α (°)	90
β(°)	90
γ(°)	90
Unit cell volume (Å^3)	4877.45(15)
Temperature (K)	153(2)
Z	4
R_1 (I>2σ(I))	0.0724
wR (all reflections)	0.2152

Ref. 4[4]. R. Banerjee, A. Phan, B. Wang, C. Knobler, H. Furukawa, M. O'Keeffe, O. M. Yaghi. High-Throughput Synthesis of Zeolitic Imidazolate Frameworks and Application to CO_2 Capture. *Science*, **2008**, 319, 939-943.

Table S3. The Content of Ir in Ir-pZCO by ICP-OES Measurement.

Element	Ir
Weight %	5.67%

Table S4. Summary of Pore Characteristics of pCO, pZCO-1, pZCO-2, pZCO-3, pZCO-4.

Samples	Surface area/m² g⁻¹ (BET)	Total pore volume[a] /cm³ g⁻¹	Micropore volume[b] /cm³ g⁻¹
pCO	25.8863	0.3042	0.0098
pZCO-1	38.4393	0.3211	0.0160
pZCO-2	65.8773	0.4956	0.0272
pZCO-3	147.3986	0.8845	0.0565
pZCO-4	35.1534	0.3300	0.0153

a At P/P0=0.99.

b Determined by NLDFT method.

Table S5. Elemental Analyses Based on EDS Results of Ir-pZCO.

C (%)		N (%)		O (%)		Zn (%)		Co (%)		Ir (%)	
Wt.	At.	Wt.	At.	Wt.	At.	Wt.	At.	Wt.	At.	Wt.	At.
6.81	9.65	19.96	24.27	58.39	62.16	3.51	0.91	9.99	2.89	1.35	0.12

Table S6. Deconvoluted Peak Position of O 1s in ZCO, pZCO, Ir-pZCO.

Sample	M-O	O_v	Ads. H_2O
ZCO	529.44 eV	531.61 eV	533.61 eV
pZCO	529.44 eV	531.61 eV	533.61 eV
Ir-pZCO	529.44 eV	531.52 eV	533.63 eV

Table S7. Deconvoluted Peak Position of Co 2p in ZCO, pZCO, Ir-pZCO.

Sample	$Co^{3+}\ 2p_{3/2}$	$Co^{2+}\ 2p^{3/2}$	$Co^{3+}\ 2p_{1/2}$	$Co^{2+}\ 2p_{1/2}$
ZCO	779.69 eV	781.59 eV	794.69 eV	796.70 eV
pZCO	779.69 eV	781.59 eV	794.69 eV	796.70 eV
Ir-pZCO	780.09 eV	781.99 eV	795.09 eV	797.10 eV

Table S8. The Summary Electrochemical Data of ZCO, pZCO, Ir-pZCO and RuO$_2$.

Sample	Overpotential (mV, η_{10})	Tafel slope (mV dec^{-1})	C$_{dl}$ value (mF cm^{-2})	Electron number (average)	charge transfer resistance (Ω)
ZCO	466	96.1	0.29	3.9725	132.9
pZCO	407	73.6	0.99	3.9510	15.1
Ir-pZCO	304	63.9	1.93	4.0017	6.4
RuO$_2$	346	69.8	/	4.0033	4.4

Table S9. The Activation Energies of ZCO, pZCO, and Ir-pZCO at Different Overpotentials.

Sample	EOER a (300 mV)	EOER a (350 mV)	EOER a (400 mV)	EOER a (450 mV)
ZCO	78.33 kJ mol^{-1}	78.17 kJ mol^{-1}	60.21 kJ mol^{-1}	43.56 kJ mol^{-1}
pZCO	73.11 kJ mol^{-1}	69.91 kJ mol^{-1}	47.82 kJ mol^{-1}	35.44 kJ mol^{-1}
Ir-pZCO	57.14 kJ mol^{-1}	35.41 kJ mol^{-1}	23.89 kJ mol^{-1}	17.85 kJ mol^{-1}

Table S10. Comparison of Various OER Electrocatalysts in Alkaline Solution.

Samples	Electrolyte	η_{10} /mV	Tafel slope /mV dec^{-1}	Ref.
Ir-pZCO	1.0 M KOH	304	63.9	**This work**
CoO$_x$-ZIF	1.0 M KOH	321	70.3	[5]
P$'_1$-Co3O4	1.0 M KOH	320	54	[6]
Fe-Co$_3$O$_4$	1.0 M KOH	384	62.9	[7]
Co$_3$O$_4$-NP-Cube	1.0 M KOH	390	50	[8]
Fractal Co$_3$O$_4$	1.0 M KOH	347	40	[9]
Co-Co$_3$O$_4$/NC	0.1 M KOH	390	65.6	[10]
Co$_3$O$_4$/Co@NCs	1.0 M KOH	323	76.4	[11]
Ir$_{0.33}$@Co$_3$O$_4$	1.0 M KOH	296	68	[12]
10-Ir-NCO	1.0 M KOH	303	78	[13]
Ir-Co$_3$O$_4$@NC	1.0 M KOH	296	89	[14]

References

1. K. Momma and F. Izumi , VESTA 3 for three-dimensional visualization of crystal, volumetric and morphology data, *J. Appl. Cryst.,* 2011, **44** , 1272-1276.

2. J. Cao , X. Zhang , S. Zhao , X. Lu and H. Ma , Mechanism of the two-dimensional $WSeTe/Zr_2CO_2$ direct Z-scheme van der Waals heterojunction as a photocatalyst for water splitting, *Phys. Chem. Chem. Phys.,* 2022, **24** , 21030-21039.

3. W. Morris , C. J. Stevens , R. E. Taylor , C. Dybowski , O. M. Yaghi and M. A. Garcia-Garibay , NMR and X-ray study revealing the rigidity of zeolitic imidazolate frameworks, *J. Phys. Chem. C,* 2012, **116** , 13307-13312.

4. R. Banerjee , A. Phan , B. Wang , C. Knobler , H. Furukawa , M. O'Keeffe and O. M. Yaghi , High-throughput synthesis of zeolitic imidazolate frameworks and application to CO_2 capture, *Science,* 2008, **319** , 939-943.

5. S. Dou , C.-L. Dong , Z. Hu , Y.-C. Huang , J.-l. Chen , L. Tao , D. Yan , D. Chen , S. Shen , S. Chou and S. Wang , Atomic-scale CoO_x species in metal–organic frameworks for oxygen evolution reaction, *Adv. Funct. Mater.,* 2017, **27** , 1702546.

6. X. Zhou , X. Liao , X. Pan , M. Yan , L. He , P. Wu , Y. Zhao , W. Luo and L. Mai , Unveiling the role of surface P–O group in P-doped Co_3O_4 for electrocatalytic oxygen evolution by On-chip micro-device, *Nano Energy,* 2021, **83** , 105748.

7. X. Wu , Z. Shao , Q. Zhu , X. Hou , C. Wang , J. Zeng , K. Huang and S. Feng , Tuning the d-Band center of Co_3O_4 via octahedral and tetrahedral codoping for oxygen evolution reaction, *ACS Catal.,* 2024, **14** ,5888-5897.

8. Z. Liu , H. M. A. Amin , Y. Peng , M. Corva , R. Pentcheva and K. Tschulik , Facet-dependent intrinsic activity of single Co_3O_4 nanoparticles for oxygen evolution reaction, *Adv. Funct. Mater.,* 2023, **33** , 2210945.

9. T. Tran-Phu , R. Daiyan , J. Leverett , Z. Fusco , A. Tadich , I. Di Bernardo , A. Kiy , T. N. Truong , Q. Zhang , H. Chen , P. Kluth , R. Amal and A. Tricoli , Understanding the activity and stability of flame-made Co_3O_4 spinels: A route towards the scalable production of highly performing OER electrocatalysts, *Chem. Eng. J.,* 2022, **429** , 132180.

10. A. K. U , A. Sethi , R. M. Lawrence and V. M. Dhavale , Co–Co_3O_4 nanostructure with nitrogen-doped carbon as bifunctional catalyst for oxygen electrocatalysis, *Int. J. Hydrogen Energy,* 2021, **46** , 34701-34712.

11. N.-F. Yu , C. Wu , W. Huang , Y.-H. Chen , D.-Q. Ruan , K.-L. Bao , H. Chen , Y. Zhang , Y. Zhu , Q.-H. Huang , W.-H. Lai , Y.-X. Wang , H.-G. Liao , S.-G. Sun , Y.-P. Wu and J. Wang , Highly efficient Co_3O_4/Co@NCs bifunctional oxygen electrocatalysts for long life rechargeable Zn-air batteries, *Nano Energy,* 2020, **77** , 105200.

12. H. Chen , S. Chen , Z. Zhang , L. Sheng , J. Zhao , W. Fu , S. Xi , R. Si , L. Wang , M. Fan and B. Yang , Single-atom-induced adsorption optimization of adjacent sites boosted oxygen evolution reaction, *ACS Catal.,* 2022, **12** , 13482-13491.

13. H.-J. Lee , D.-H. Park , W.-J. Lee , S.-B. Han , M.-H. Kim , J.-H. Byeon and K.-W. Park , Mesoporous spinel Ir-doped $NiCo_2O_4$ nanostructure as an efficient catalyst for oxygen evolution reaction, *Appl. Catal. A-Gen.,* 2021, **626** , 118377.

14. S. Jung , R. A. Senthil , C. J. Moon , N. Tarasenka , A. Min , S. J. Lee , N. Tarasenko and M. Y. Choi , Mechanistic insights into ZIF-67-derived Ir-doped Co_3O_4@N-doped carbon hybrids as efficient electrocatalysts for overall water splitting using in situ Raman spectroscopy, *Chem. Eng. J.,* 2023, **468** , 143717.